Supporting Information

Chiral Nanohole Arrays

Bin Ai,[†*] *Hoang M Luong*,[†] *Yiping Zhao*

[†] These authors contribute equally to this work

Prof. B. Ai,
School of Microelectronics and Communication Engineering, Chongqing University, Chongqing P.R. China, 400044
Chongqing Key Laboratory of Bio-perception & Intelligent Information Processing, Chongqing, P.R. China, 400044
H.M. Luong, Prof. Y. Zhao
Department of Physics and Astronomy, University of Georgia, Athens, Georgia 30602, United States
Email: binai@cqu.edu.cn

Section SI. MATLAB Model

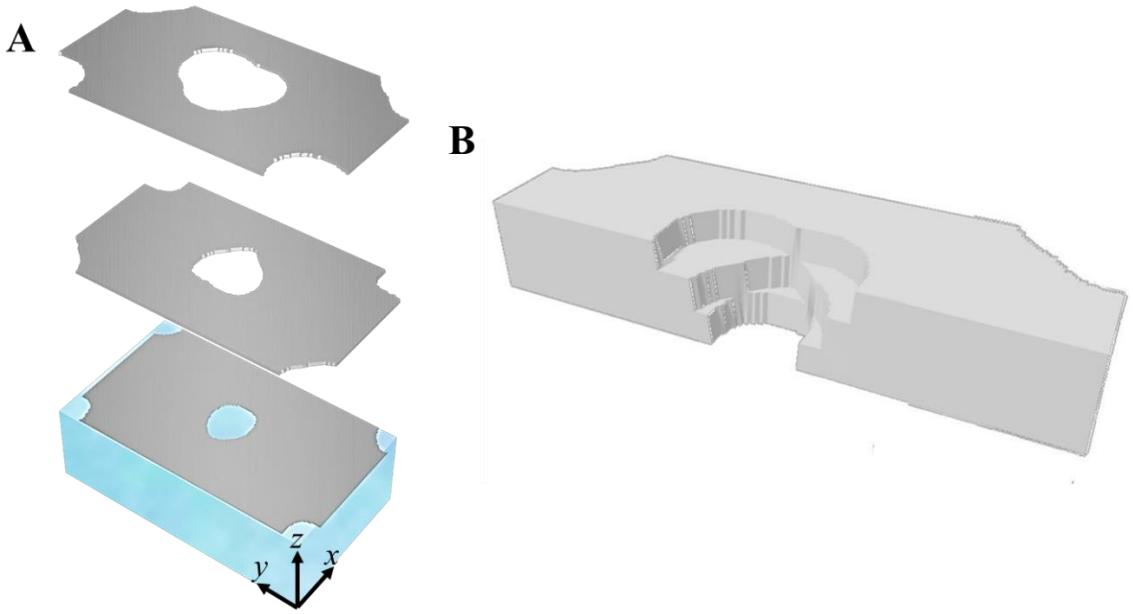

Figure S1. (A) Schematic of the plane section of the LH-CNA. The bottom, middle, and top planes are at t = 0 (Ag/glass interface), 30, and 70 (Ag/air interface) nm, respectively. (B) Cross-section of the LH-CNA model calculated by the MATLAB program. The edge is sharp and the layers are clearly separated.

Section SII. Calculation of Local Current Density

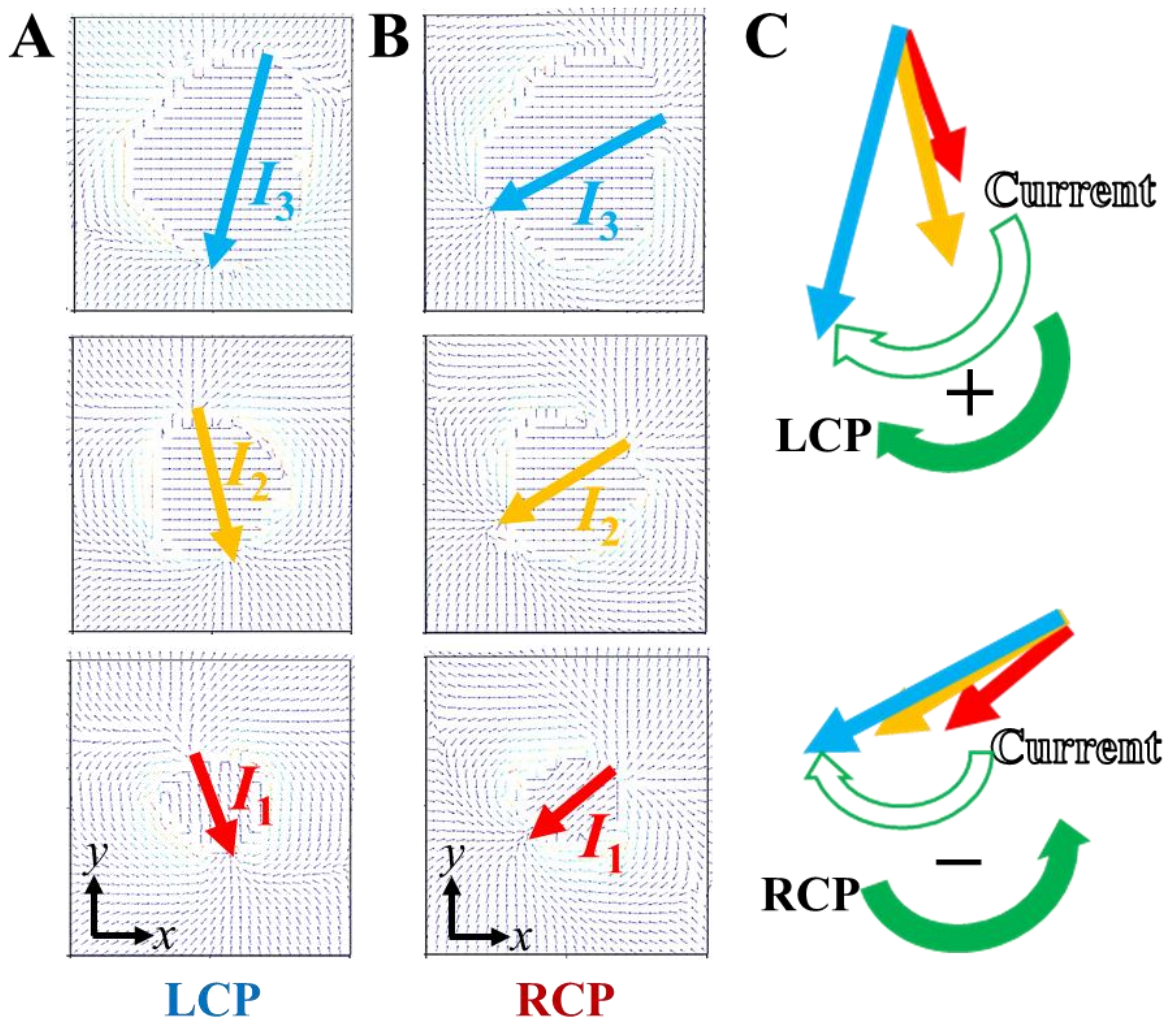

Figure S2. The local electron current distributions in the bottom, middle, and top planes of the LH-CNA excited by the (A) LCP and (B) RCP incident light at λ_1 = 739 nm. The planes correspond to those in Figure S1A. The arrows show the direction from positive current pole to negative current pole. (C) Top-view illustration of propagation of effective current pole directions from the bottom layer to the top layer under LCP and RCP illuminations, respectively. The straight arrows indicate the pole direction, which are extracted from (A) and (B).

In order to reveal the mechanism of the chiro-optical response, the local current density

distributions induced by incident RCP and LCP lights for the LH-CNA at the SPP peak λ_1 were calculated based on the MATLAB model in **Figure 1A**. **Figure S1A** shows the three planes of the oval holes produced in the model at the Ag thickness t = 0, 30, and 70 nm, respectively. **Figure S2A** and **S2B** show the calculated current densities in each plane under the LCP and RCP lights at λ_1 = 739 nm. As shown in **Figure S2A** and **S2B** , in each plane, two current sources are visible, *i.e.*, the positive and the negative poles, as effectively depicted by I_1 (bottom layer, red arrow), I_2 (middle layer, yellow arrow), and I_3 (top layer, blue arrow), and the pole direction pointing from the positive pole to the negative pole is changing along the propagation direction of the incident light, The effective pole directions in the three planes are different for the LCP and RCP incidence, which is attributed to the different phases of incident light with different polarizations. For both LCP and RCP incident lights, the directions of I_1, I_2, and I_3 exhibit the same relative in-plane rotation. The rotation angles under LCP are 7° and 29° for I_1 to I_2 and I_2 to I_3, respectively (**Figure S2A**). The rotation angles under RCP are smaller, with 6° and 3°, respectively (**Figure S2B**). The relative in-plane rotation of the pole directions is the same as the rotation of the polarization direction for LCP incidence and opposite to that for the RCP incidence, as depicted in **Figure S2C**.

The chiro-optical response in transmission can be understood based on the process of light propagation though the NAs and the Born−Kuhn model. The Born−Kuhn model is one of the most intuitive ways to understand the generation of natural optical activity in chiral media, which is demonstrated based on two identical, vertically displaced, and coupled oscillators.[1]

If the orientation of the two particles is different, the coupling between the two particles will set the second oscillator oriented differently compared to the original polarization, thus leading to a polarization rotation. For the NAs, the periodicity allows the coupling of light to the structure in the form of SPPs. SPPs on the light incident interface couple evanescently to the light transmitted interface before being re-emitted into freely propagating mode. The role of SPPs is to enhance the field amplitudes around the apertures which then compensates for the exponential attenuation of the evanescent field in the depth of the non-propagating aperture. Therefore, the transmission spectra of such structures are characterized by a set of peaks corresponding to the appearance modes. In our CNAs, the symmetric coupling between the handedness of the structure and polarization of the light, *i.e.*, with the same rotation, would compensate more to the evanescent field, thus leading to higher transmission (the top schematic in **Figure S2C**). The opposite rotation between the handedness of the structure and polarization would weaken the evanescent field and in turn reduce the transmission (the bottom schematic in **Figure S2C**). The oscillation model in this work can be analogical to the classic Born−Kuhn model by regarding the CNAs as three separated NAs with different orientation. The Born-Kuhn model is based on LSPR of particles, while we use thin films instead of particles and develop the model from LSPR to SPP. LSPR can also be excited at the hole edges or at random defects,[2] however, does not show significant CD effects in this calculation.

Section SIII. Effect of Thickness on Chiral-Optical Response

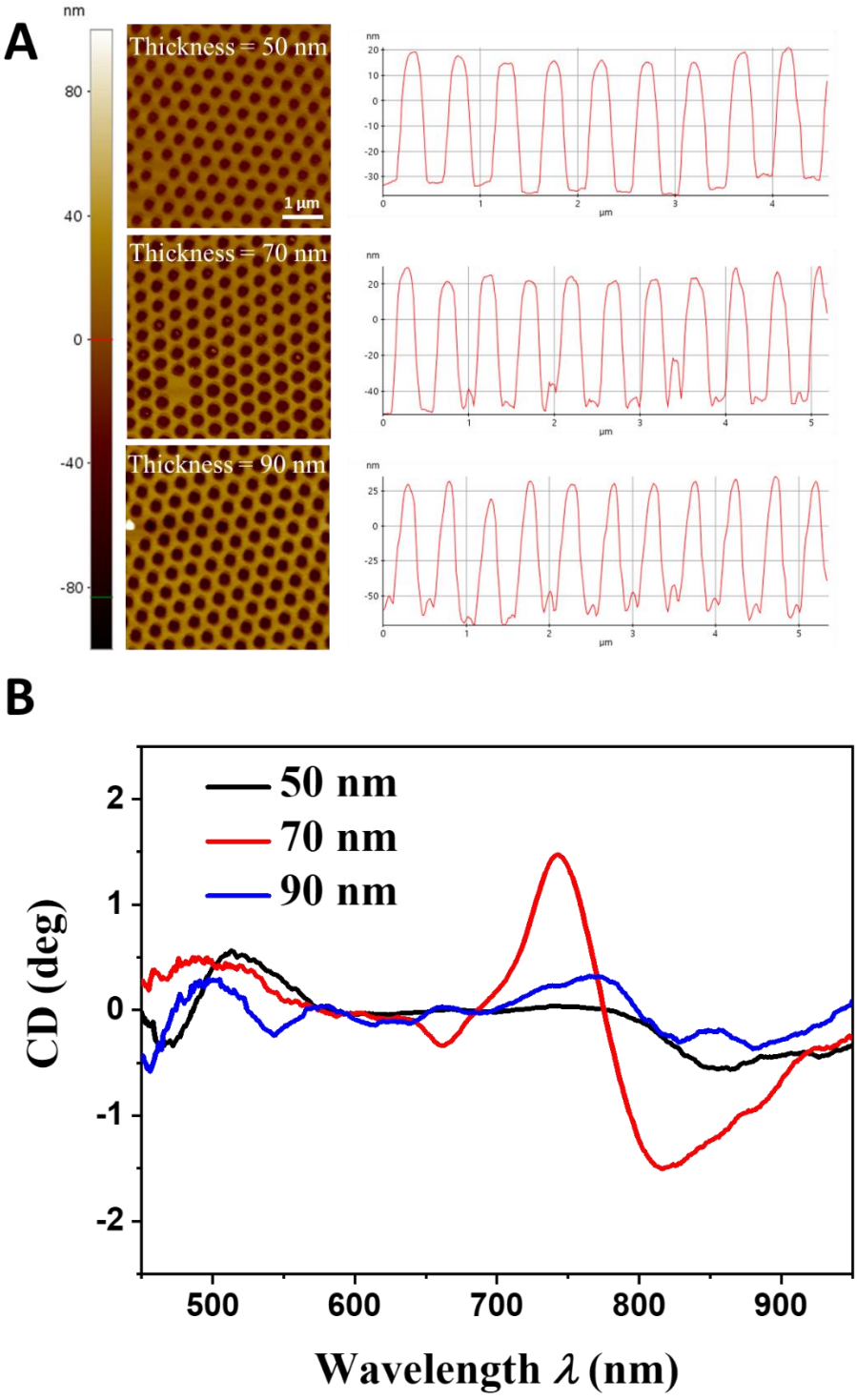

Figure S3. (A) AFM images and section profiles of the CNAs with thickness of 50, 70, and 90 nm. (B) The CD spectra of the CNAs with thickness of 50, 70, and 90 nm.

CNAs with thickness of 50 and 90 nm were fabricated. The section profiles of the CNAs with different thicknesses are shown in **Figure S3A**. Their ΔT spectra are shown in **Figure S3B**. The CNA with thickness of 70 nm shows the strongest chiral-optical response.

Section SIV. Effect of Oblique Incident Light on Chiral-Optical Response

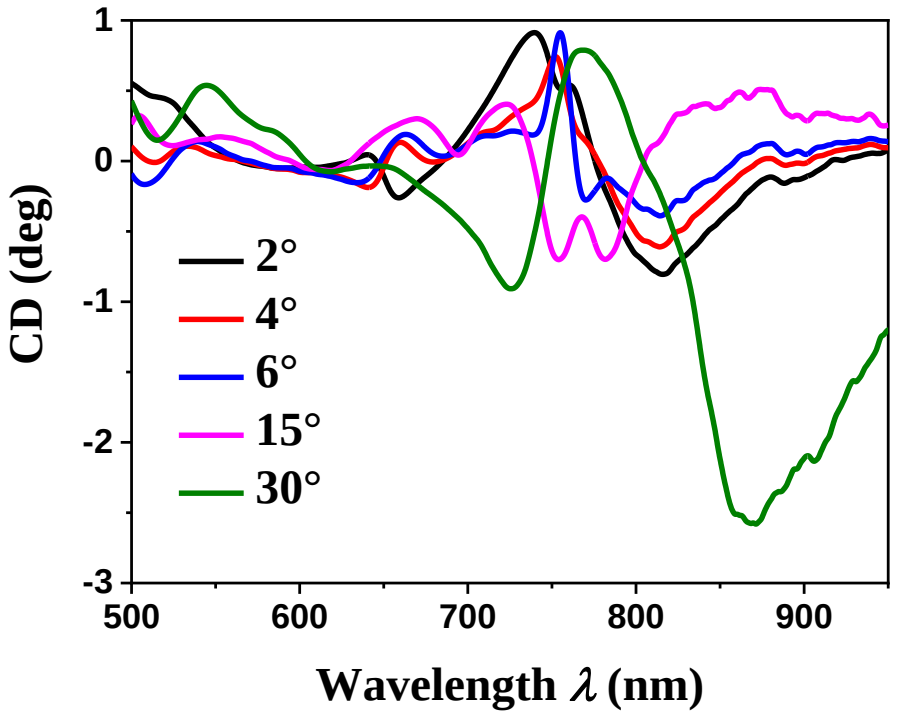

Figure S4. The CD spectra of the LH-CNA with the incident angle of 2°, 4°, 6°, 15°, and 30°.

Angle-resolved CD spectra were measured and shown in **Figure S4**. The chiral-optical response changes with incidence angle. The spectral profile with small angle (≤ 6°) is similar to that (**Figure 2F**) with normal incidence. Whereas the CD signal changes much with incidence angle of 15° and 30°. The oblique incidence trigger more asymmetric factors, leading to complicated chiral-optical response. The effect of oblique incidence needs to be further studied, which is beyond the scope of this work.

Section SV. Polar Plots of $\Delta\alpha$

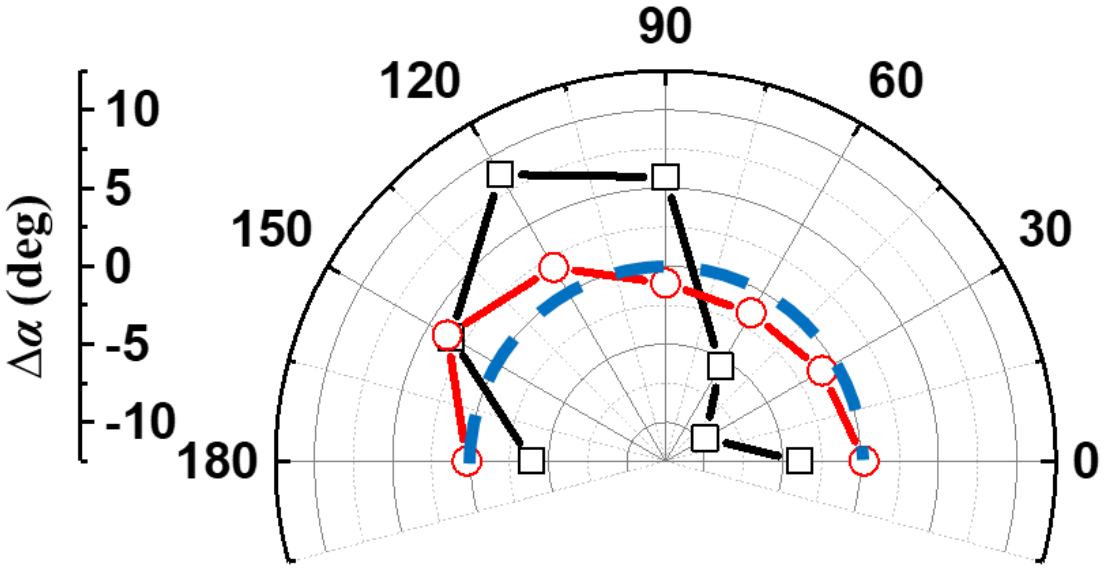

Figure S5. Polar plots of $\Delta\alpha$ at λ = 696 (black curve and symbol) and 743 nm (red curve and symbol). The blue curve indicates $\Delta\alpha = 0$.

Section SVI. Domain Dependence of Chiro-Optical Response

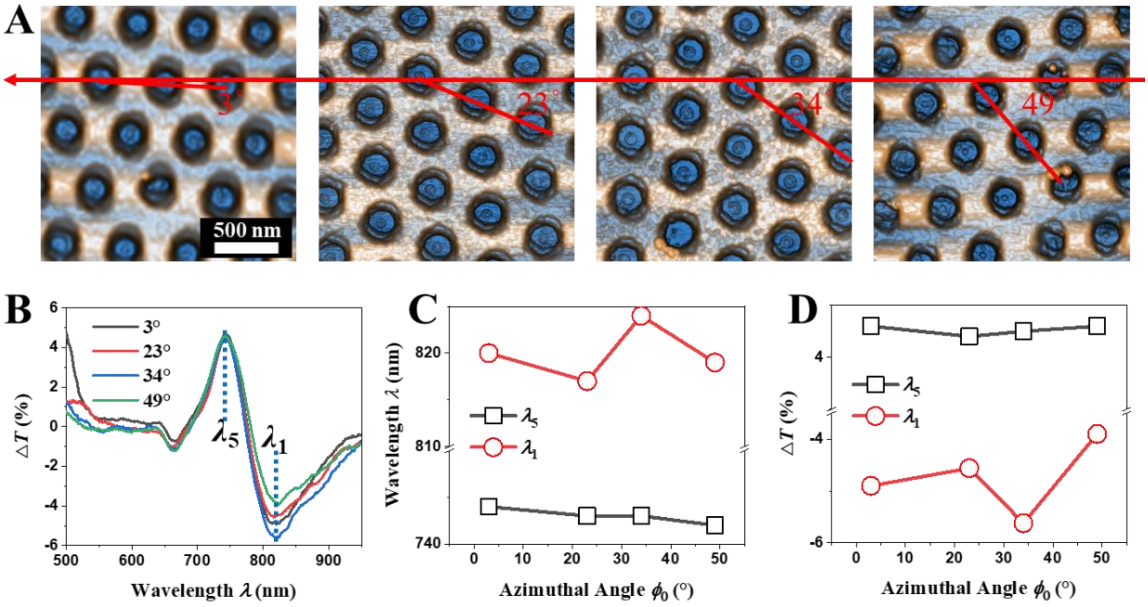

Figure S6. (A) AFM images of the LH-CNAs for different monolayer domains. (B) The experimental ΔT of a LH-CNA sample at different domains corresponding to those in (A). The plots of the (C) peak and valley location and (D) ΔT at λ_1 and λ_5 versus the domain orientation angle ϕ_0.

As shown in **Figure S6A**, LH-CNAs with different domains can be found in one sample. The red horizontal arrows indicate the first deposition direction (initial azimuthal angle). The angle between the lattice orientation and the initial azimuthal angle changes in different domains. **Figure S6B** shows the measured ΔT spectra of those domains in **Figure S6A**. The standard deviation of the peak/dip wavelength for λ_5 and λ_1 is 0.8 nm and 2.9 nm, respectively (**Figure S6C**). The standard deviation of the peak/dip intensity for λ_5 and λ_1 is 0.095 % and 0.72 %, respectively (**Figure S6D**). The correlation coefficient of the four spectra is around 0.99. Clearly, the change of ΔT spectra in different domains are small, and are within the

error bar. Thus, the chiral properties of the CNAs are independent on the domains, *i.e.*, the entire sample shows uniform CD response.

Section SVII. Calculation of Superchiral Fields

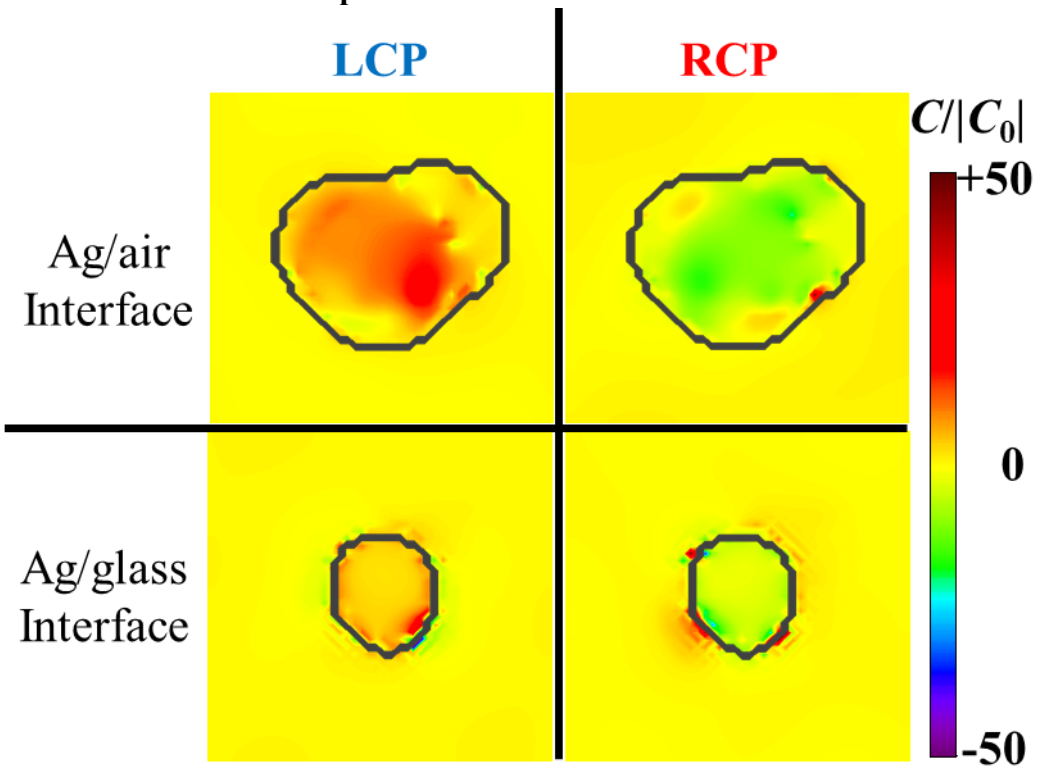

Figure S7. Superchiral fields $|C/C_0|$ of the LH-CNAs excited by LCP and RCP incident light at λ_1 = 739 nm based on the MATLAB model. The top and bottom panels show the Ag/air and Ag/glass interface, respectively. The black curves show the outlines of the nanoholes.

Section SVIII. Chiro-Optical Response in Buffer Solution

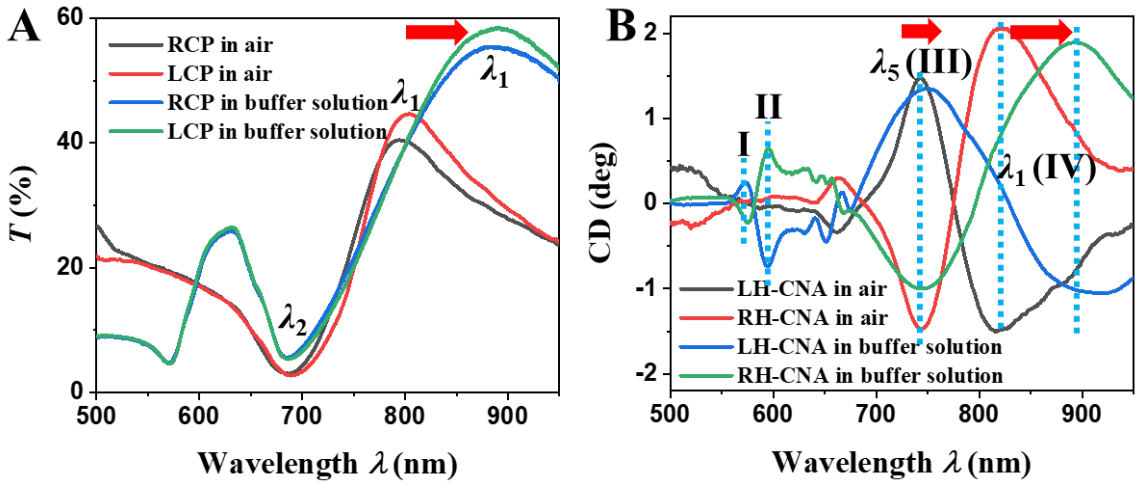

Figure S8. (A) $T_L(\lambda)$ and $T_R(\lambda)$ of the LH-CNAs in air and buffer solution. (B) The CD spectra of the LH- and RH-CNAs in air and buffer solution.

As shown in **Figure S8A**, $T_L(\lambda)$ and $T_R(\lambda)$ of the LH-CNAs in air and buffer solution show the similar spectra features with a peak at λ_1 and a valley at λ_2. The λ_1 red shifts ~ 90 nm from air to buffer solution, while λ_2 stays almost at the same wavelength. This is because λ_1 is the SPP peak which has robust response to the change of surrounding environment and λ_2 is due to the non-resonant Wood anomaly. The red-shift of the $T_L(\lambda)$ and $T_R(\lambda)$ leads to the red-shift of the CD spectra, as shown in **Figure S8B**. The shift of λ_5 is only 10 nm, which is much smaller than that of λ_1 (~ 70 nm). The reason is that λ_5 is excited by LSPR whose sensitivity is usually lower than that of SPP (λ_1).

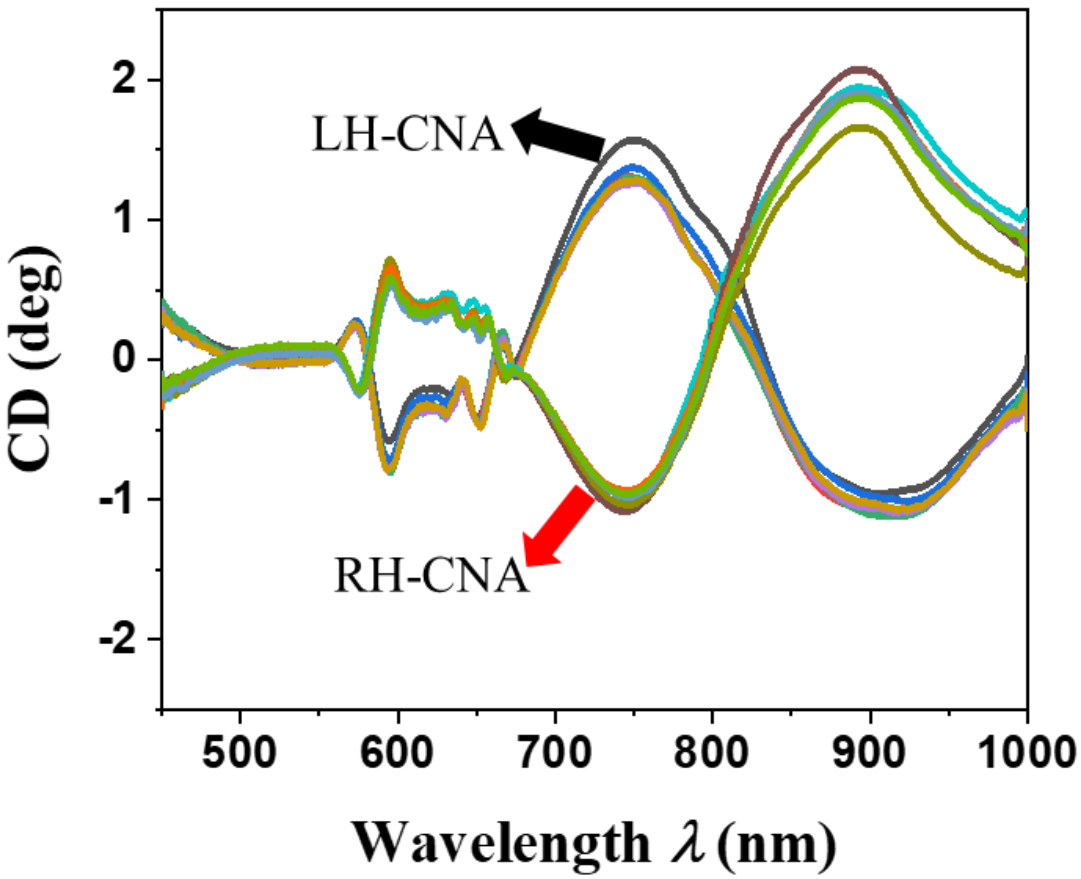

Figure S9. The CD spectra of the LH- and RH-CNAs in buffer solution with six measurements at different sample locations.

Section SIX. Chiro-Optical Response in IPA

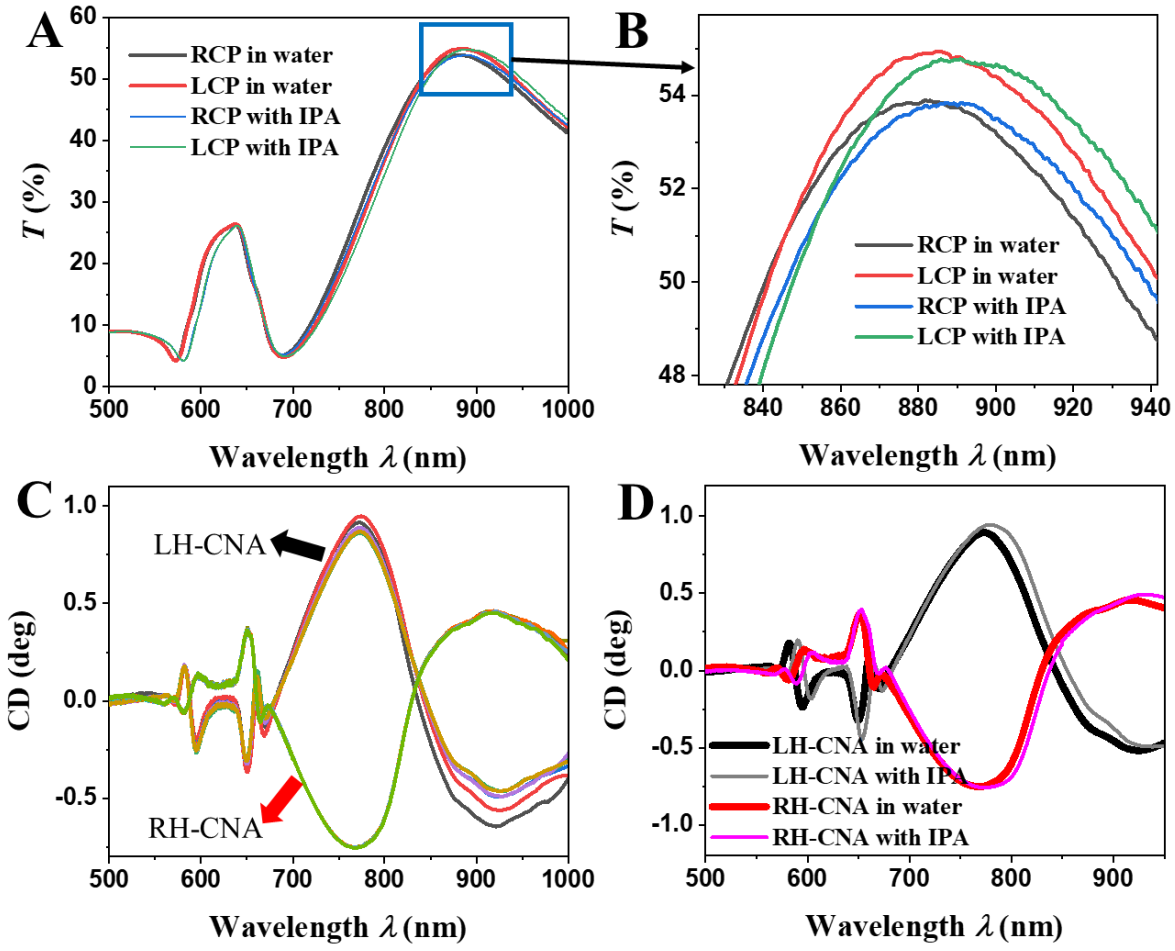

Figure S10. (A) The $T_L(\lambda)$ and $T_R(\lambda)$ of the LH-CNAs in water and in 0.085 M IPA mixed with water. (B) The zoomed in $T_L(\lambda)$ and $T_R(\lambda)$ in the rectangle in (A). (C) The CD spectra of the LH- and RH-CNAs in water with six measurements at different sample locations. (D) The averaged CD spectra of the LH- and RH-CNAs in water and in 0.085 M IPA.

The $T_L(\lambda)$ and $T_R(\lambda)$ of the LH-CNAs in water and in 0.085 M IPA are similar to those in buffer solution, as shown in **Figure S10A**. The peaks in $T_L(\lambda)$ and $T_R(\lambda)$ red shift when the solution is changed from water to IPA due to the increase of n (**Figure S10B**). The measurements at different locations and samples are consistent, indicating the good

reproducibility (**Figure S10C**). In addition, the modes I, II, III, and IV appear in all the CD spectra measured at different locations, different samples, and in different solvent (buffer solution, water, water with IPA). This demonstrates the four modes are convinced chiro-optical responses.

Section SX. Chiro-Optical Response for Detecting ThD

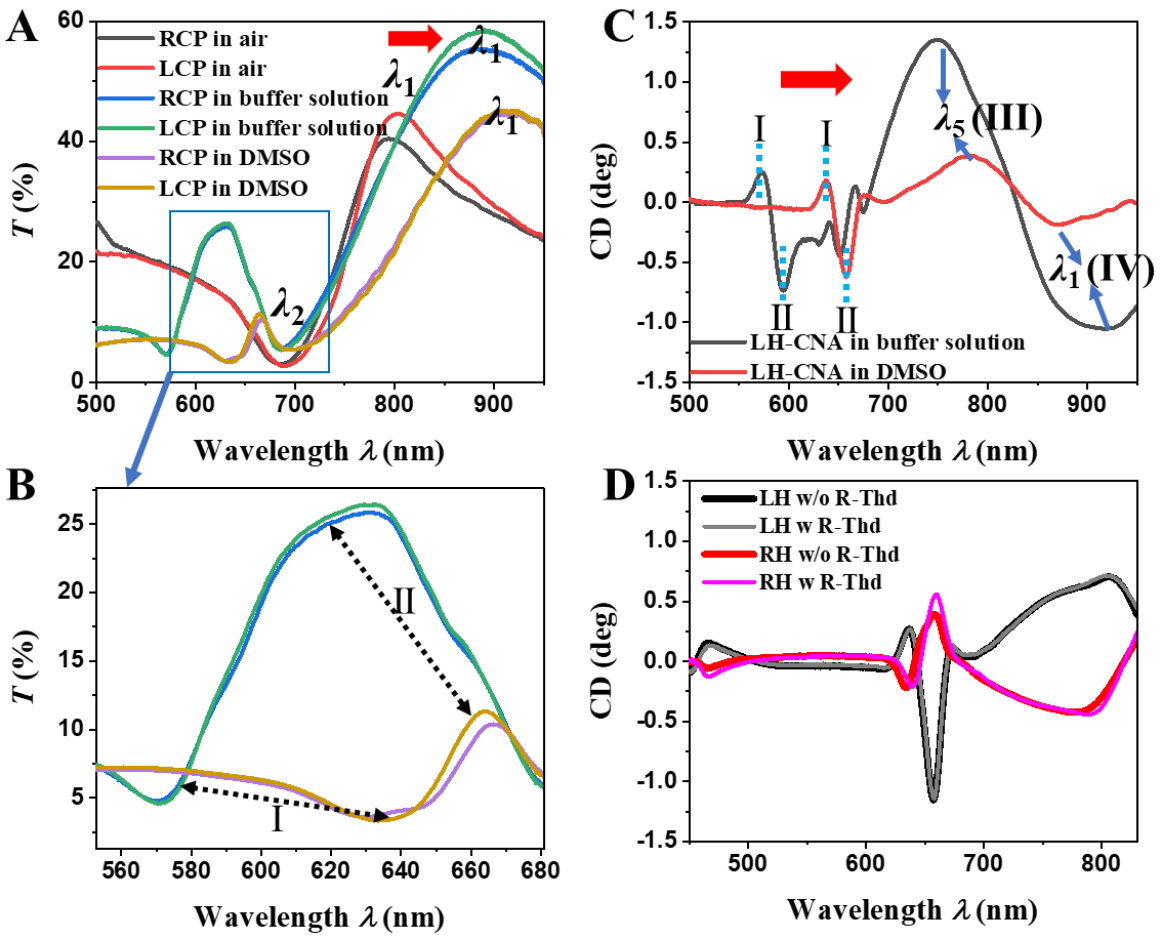

Figure S11. (A) The $T_L(\lambda)$ and $T_R(\lambda)$ of the LH-CNAs in air (n = 1), buffer solution for ConA ($n \approx 1.33$), and DMSO (n = 1.48). (B) The zoomed-in $T_L(\lambda)$ and $T_R(\lambda)$ in the rectangle in (A). The arrows indicate the area where the modes I and II are generated. (C) The CD spectra of the LH-CNAs in buffer solution and DMSO. (D) The CD spectra of the LH-and RH-CNAs with and without R-ThD.

The $T_L(\lambda)$ and $T_R(\lambda)$ in DMSO show the similar profile to those in air and buffer solution for ConA. The red shift of λ_1 is due to the increase n of the solvent. The λ_2 does not change much because it is induced by the Wood anomaly. There are differences between $T_L(\lambda)$ and $T_R(\lambda)$ in

buffer solution and DMSO (**Figure S11B**) in the wavelength range of 550 – 680 nm, where the modes I and II are generated. The CD responses generated in this wavelength region demonstrate the same modes, *i.e.*, the four modes I, II, III, and IV (**Figure S11C**). Note that the chiro-optical response in DMSO is weaker than that in buffer solution Since the index contrast between DMSO and glass is smaller, i.e., $n_{DMSO} = 1.48$, which is closer to $n_{glass} = 1.5$. Since λ_1 is excited by the local current rotation at the top and bottom interfaces and thus mainly depends on the index mismatch. The weaker index mismatch would have more effects on λ_1, which may be responsible for the blue-shift of the λ_1 (mode IV) in **Figure S11C**. Other modes are excited by either LSPR or higher-order SPP, which are mostly due to the intrinsic mirror symmetry breaking and are less affected by the index matching. From this point of view, the modes I, II, and III are qualified as the good tracking features for sensing.

References

1. X. Yin, M. Schäferling, B. Metzger and H. Giessen, *Nano Lett*, 2013, **13**, 6238-6243.
2. A. Degiron and T. W. Ebbesen, *J Opt a-Pure Appl Op*, 2005, **7**, S90-S96.